Resonance Raman De-Enhancement Caused by Excited State Mixed Valence

Xianghuai Wang,[†] **Guadalupe Valverde-Aguilar,**[†,§] **Michael N. Weaver,**[‡]
Stephen F. Nelsen,[*,‡] **and Jeffrey I. Zink**[*,†]

*Department of Chemistry and Biochemistry, University of California, Los Angeles, California 90095, and
Department of Chemistry, University of Wisconsin, 1101 University Avenue, Madison, Wisconsin 53706-1396*

Resonance Raman and absorption spectra of 9,10-bis(2-*tert*-butyl-2,3-diazabicyclo[2.2.2]oct-3-yl)-anthracene
(**2**) are measured and analyzed. The contribution of the individual vibrational normal modes to the reorganization
energy is investigated. Excited-state mixed valence in this system is analyzed using density functional theory
electronic structure calculations. The resonance Raman excitation profiles exhibit a resonance de-enhancement
effect around 20 725 cm^{-1}, but a corresponding feature is not observed in the absorption spectrum. This
unusual observation is attributed to the presence of a dipole-forbidden, vibronically allowed component of
the split mixed valence excited state. The de-enhancement dip is calculated quantitatively and explained in
terms of the real and imaginary components of the polarizabilities of the two overlapping excited states.

Introduction

Photoinduced electron-transfer is a broad subject that has been
recently reviewed.[1−3] Absorption of a photon by a donor−
acceptor (D−A) system can produce an excited state that has
an amount of charge-transfer varying from very little to almost
complete, and thermal electron transfer may also follow
photoexcitations that produce little charge transfer in the initial
step to yield a charge-separated product state indirectly. Several
of the spectroscopic techniques that are used to study electron
transfer upon photoexcitation have been reviewed.[4] In
this paper we use electronic absorption spectroscopy, resonance
Raman (rR) spectroscopy, and the time-dependent theory of
spectroscopy[5−12] to analyze the photoinduced electron-transfer
in aryl dihydrazine **2**, which is compared with monohydrazine
1,[13] which was previously studied by rR.[14]
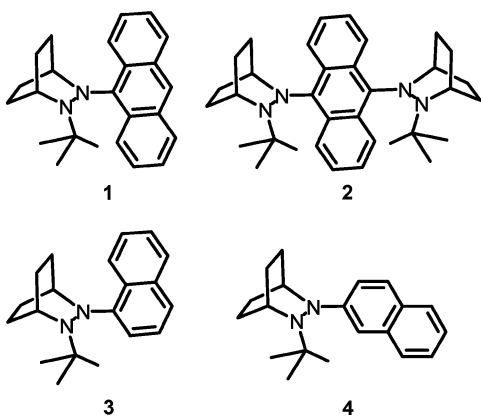
1 and **2** have 2-tert-butyl-3-azabicyclo[2.2.2]octy-3-yl (**Hy**) D
groups attached respectively at the 9- and 9,10- positions of

* Corresponding authors. E-mail: zink@chem.ucla.edu.
† University of California, Los Angeles.
‡ University of Wisconsin.
§ Current address: Instituto de Física, UNAM, Departamento de Estado
Sólido, Ciudad Universitaria, Del. Coyoacán, P.O. Box 20-364, 01000,
México, D.F. México.

anthracene, which acts as A. Charge separation upon photoex-
citation in the neutral forms of **1** and hydrazine-substituted
naphthalenes **3**, **4**, and four related bishydrazine compounds has
been studied previously using electrooptical absorption and
fluorescence spectroscopy.[15] The **Hy** group has been extensively
used as a conveniently stable high reorganization energy charge-
bearing unit that allows ESR determination of intramolecular
electron-transfer rate constants between the **Hy** units for **Hy₂Ar**$^+$
intervalence radical cations that have a large enough electronic
coupling to allow accurate determination of the electron-transfer
parameters using Hush theory.[16,17] Examples with five,[18−20]
seven,[21] and nine[20,22] bonds between the charge-bearing units
have been found to have electron-transfer rate constants that
are accurately predicted using Hush theory.[23] In contrast, the
radical cation **2**$^+$ showed much faster electron-transfer than
predicted, and two bridge-to-Hy$^+$ transitions for it lie below or
near the Hy-to-Hy$^+$ intervalence transition, which causes the
two-state model that suffices for several other systems to break
down.[13] This work reports unusual effects on photoelectron
transfer for the neutral oxidation level of **2** as well.

Compound **2** is an excited-state mixed valence (ESMV)
system. ESMV occurs for molecules which have symmetrical
ground states but two or more equivalent donor (D) or acceptor
(A) sites attached to a bridge (B), for which charge-transfer
occurs upon photoexcitation. **2** is a neutral D−B−D example,
which has equal energy diabatic excited states that may be
usefully described as D$^+$-B$^-$-D and D−B$^-$-D$^+$. Other ESMV
systems that we have studied include the naphthalene-bridged
analogues of **2**,[15] and several open-shell examples, including a
durene-bridged diradical dication,[24] delocalized intervalence
compounds including a variety of dinitroaromatic radical
anions,[25] 9-bond-bridged diamine radical cations,[26] diarylhy-
drazine radical cations,[27−29] and a ruthenium-bridged dipyridine
dication.[30] The neighboring orbital theory used for a more
quantitative analysis of ESMV systems (see below) has also
been presented.[31] The lowest-energy absorption band for an
ESMV compound in principle consists of two components, but

5442 *J. Phys. Chem. A, Vol. 111, No. 25, 2007*

Wang et al.

their relative absorptivities are determined by the angle between the charge-bearing unit to bridge transition dipole moments. Because **2** has a 180° angle between these dipole moments, only one of the components is allowed and observed.

In this paper, we report the absorption spectra and the rR excitation profiles taken in resonance with the lowest energy absorption band of **2**. The highly distorted vibration modes are identified and assigned by using density functional theory (DFT) calculations. The excited-state distortions, Δ, are calculated using time-dependent theory. The contributions of individual modes to the reorganization energy are investigated and compared with those of **1**. An unusual resonance de-enhancement effect was found in the rR excitation profiles that is caused by the overlap of the two components of the mixed valence excited state. The two components of the ESMV overlap and produce a single broad featureless band in the absorption spectrum, but are revealed in the excitation profiles. The excitation profiles, including the de-enhancement dip, are calculated quantitatively and the origin of the dip is explained. The energy separation and thus the coupling cannot be determined from the absorption spectrum but are revealed by the excitation profiles.

Experimental Section

The preparation of **2** has been previously reported.[13]

Electronic Spectroscopy. Absorption spectra of **2** were obtained at room temperature in toluene solution and in a Halogrease mull using a Cary 5000 UV−vis−NIR spectrophotometer.

Raman Spectroscopy. Raman spectra of **2** were obtained using a 1401 Spex double monochromator equipped with a Burle C31034 photomultiplier tube, a Stanford Research System SR400 photon counter and processed by a PC computer, or by using a triple monochromator and detected by a CCD. Excitation was provided by an argon laser (for wavelengths of 514.5, 488.0, 476.5, 472.7, 465.8, and 457.9 nm) and a krypton laser (for wavelengths of 482.5, 530.9, 568.2, 647.1, and 676.4 nm). Interference filters (488.0 and 457.9 bandpass) were used with 488.0 and 457.9 nm excitations, respectively, to eliminate plasma lines. Additional excitation wavelengths of 586.1, 604.6, and 611.4 nm, were obtained using a Rhodamine 6G dye laser.

Spectra were collected from spinning pellets made from a finely ground mixture of **2** and the reference compound $NaNO_3$ at a ratio of 1:0.03. The Raman intensities were obtained by numerically integrating the peaks.

Theoretical and Numerical Methods

The time-dependent theory[32−41] is used because it is easy to visualize qualitatively and to calculate quantitatively the spectroscopic consequences of coupling states. In the time dependent theory, the Raman intensity $I_{i \rightarrow f}$ into a particular mode f is

$$I_{i \rightarrow f} \propto \omega_I \omega_S{}^3 |\alpha_{fi}|^2 \qquad (1)$$

where $\hbar \omega_I$ is the energy of the incident radiation, $\hbar \omega_S$ is the energy of the scattered radiation, and α_{fi} is the resonance Raman scattering polarizability, which can be given by

$$\alpha_{fi} = \frac{i}{\hbar} \int_0^\infty \langle \phi_f | \phi(t) \rangle \exp\{i(\omega_i + \omega_I)t - \Gamma t\} \, dt \qquad (2)$$

In eq 2, $|\phi_f\rangle = \mu|\chi_f\rangle$ is the final vibrational state of the ground electronic surface, χ_f, multiplied by the transition electric dipole moment μ, $|\phi(t)\rangle = \exp(-i\hat{H}t/\hbar)|\phi\rangle$ is a moving wave packet where $|\phi\rangle$, the wave function of initial state, is multiplied by
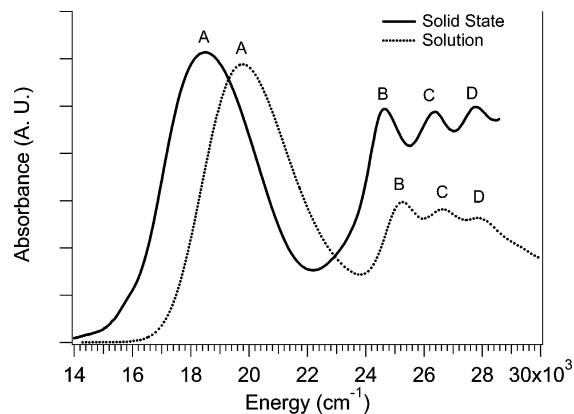

Figure 1. Absorption spectrum of **2** in a Halogrease mull (solid line) and in toluene (at 1.6×10^{-4} M) (dotted line) at room temperature.

the electronic transition dipole moment and propagated on the excited-state by the excited-state Hamiltonian, $\hbar \omega_i$ is the vibrational zero-point energy of the ground electronic state surface, and Γ is the damping factor. For simplicity, in this paper the transition moments μ are chosen to be coordinate independent, i.e., constants.

The propagating wavefunction $\phi(t)$ is calculated by the split operator method developed by Feit and Fleck.[42−44] The Hamiltonian is

$$\hat{H} = -\frac{1}{2} M \nabla^2 + V(Q) \qquad (3)$$

where V(Q) is the potential energy as a function of normal mode coordinate Q and $(-1/2)M\nabla^2$ is the nuclear kinetic energy. In Feit and Fleck's method, both the coordinate Q and the time t are represented by grid points which have the intervals ΔQ and Δt, respectively. The time-dependent wavefunction $\phi(Q,t+\Delta t)$ can be obtained from $\phi(Q,t)$ using the equation

$$\phi(Q,t+\Delta t) = \exp\left(\left(\frac{i\Delta t}{4M}\right)\nabla^2\right) \exp(i\Delta tV) \exp\left(\left(\frac{i\Delta t}{4M}\right)\nabla^2\right)\phi(Q,t) +$$
$$O[(\Delta t)^3] = \hat{P}\hat{V}\hat{P}\phi(Q,t) + O[(\Delta t)^3] \quad (4)$$

In the remainder of this paper, the symbol ω (cm^{-1}) is used to represent the vibrational wavenumber. It is related to the angular frequency ω (s^{-1}) by ω (cm^{-1}) = $[\omega(s^{-1})]/2\pi c$.

Results

Absorption Spectroscopy. The absorption spectra of **2** in toluene solution and as a solid in a Halogrease mull are shown in Figure 1. The solution spectrum has a charge-transfer maximum at 19 760 cm^{-1} and anthracene-centered π,π^* absorption bands at 25 250, 26 670, and 27 890 cm^{-1} (labeled B, C, and D, respectively). In the solid-state spectrum these bands shift to lower energy. The transition energies are summarized in Table 1.

Resonance Raman Spectroscopy. Raman spectra obtained at two excitation wavelengths, 514.5 nm (19 435 cm^{-1}, the wavenumber in air, near the maximum of the charge-transfer band) and 472.7 nm (21 155 cm^{-1}, the wavenumber in air, near the minimum between the bands) are shown in Figure 2. The intensities of the Raman peaks of **2** relative to those of the standard (1067 and 725 cm^{-1}) decrease when the excitation wavelength is changed from 514.5 to 472.7 nm. Table 2 lists all of the peaks with intensities of a least 10% of that of the most intense sample peak (1398 cm^{-1}) observed in the resonance Raman spectrum taken at the maximum in the excitation profile.

Resonance Raman De-Enhancement

J. Phys. Chem. A, Vol. 111, No. 25, 2007 **5443**

TABLE 1: Comparison of the Absorption Spectra of 1 and 2

compound	E_{a1} toluene	E_{a1} (ϵ_{max}) CH$_2$Cl$_2$	E_{a1} KBr	E_{a2} toluene	E_{a2} KBr
HyAN(**1**)^a	21830	21510 (3780)^b	21230	26390	25970
				27860	27250
Hy$_2$AN(**2**)	19760	19610 (6030)	18480	25250	24630
				26670	26390
				27890	27780
ΔE_{a1}(**1−2**)	2070	1900	2750	1140	

^{a} Ref 13. ^{b} From the thesis of R. F. Ismagilov, University of Wisconsin, 1998.
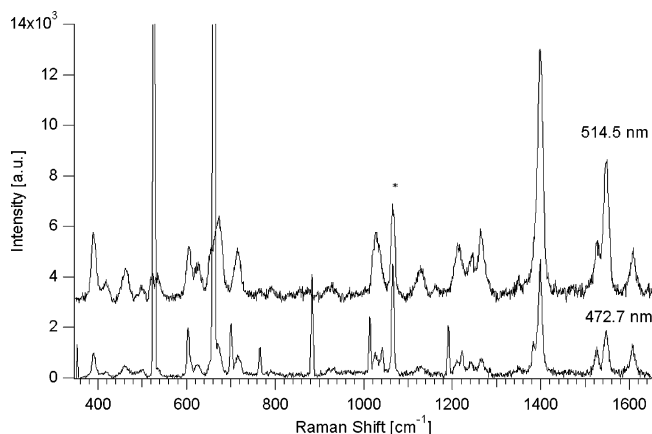

Figure 2. Raman spectra of **2** using (a) 514.5 and (b) 472.7 nm excitation. The peak labeled with * at 1067 cm^{-1} is a NaNO$_3$ reference peak.

TABLE 2: Raman Frequencies, Distortions, and Assignments

ω_{exp} (cm^{-1})	$I_{ratio}{}^a$	Δ	ω_{calc} (cm^{-1})	assignment^b
390	2.30	1.04	389	in plane AN def
417	1.11	0.67	414	out of plane AN def
462	3.15	1.02	458	out of plane AN def
606	2.20	0.65	614	in plane AN def + AL C−NNC def
626	1.38	0.5	637	in plane AN def + AL C−NNC def
673	4.50	0.84	669	C−NN−C def
715	1.98	0.59	708	NN str. + AL C−NNC def
1026	2.64	0.42	1029	AN C−N str. + in plane AN def
1036	1.83	0.35	1030	NN str. + AL C−NNC def
1130	2.69	0.39	1136	in plane AN def
1242	3.23	0.39	1252	AN CC str.
1265	4.29	0.44	1265	AN CC str.
1398	8.60	0.56	1391	AN C−N str. + AN CC str.
1527	2.45	0.27	1536	AN CC str.
1547	5.38	0.40	1560	AN CC str. + AN C−NN bend
1607	2.36	0.26	1627	AN CC str.

^{a} Intensity ratio for each mode in the 530.9 nm spectrum to that of the standard NaNO$_3$ peak at 1067 cm^{-1}. ^{b} AL = aliphatic bicycle[2.2.2]octane group; AN = anthracene; def = deformation; str. = stretch

The intensity ratio for each mode in the 530.9 nm excitation Raman spectrum to that of the standard NaNO$_3$ peak at 1067 cm^{-1} are also listed in Table 2.

Plots of the integrated Raman intensities as a function of the excitation energy (the resonance Raman excitation profiles) are shown in Figure 3, in which the eight modes with the largest distortions are plotted. The resonance Raman excitation profiles were obtained using 14 laser wavelengths (676.4, 647.1, 611.4, 604.6, 586.1, 568.2, 530.9, 514.5, 488.0, 482.5, 476.5, 472.7, 465.8, and 457.9 nm).
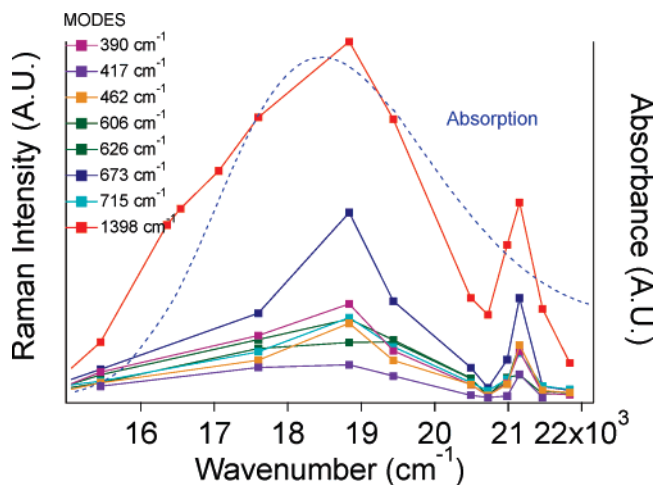

Figure 3. Resonance Raman excitation profiles of the eight most enhanced modes for 9,10-bis(2-tert-butyl-2,3-diazabicyclo[2.2.2]oct-3-yl)anthracene.
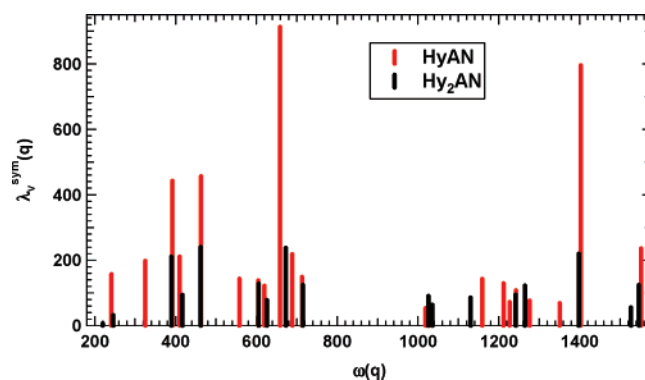

Figure 4. Contribution of the individual vibrational modes to the reorganization energy for **1** (red bars) and **2** (black bars). The units of ω and λ_v^{sym} are both in cm^{-1}.

Discussion

1. Resonance Raman Spectra. The vibrational modes that appear in the resonance Raman spectra were assigned using a B3LYP/6-31G* calculation carried out with Gaussian 03.[45] The experimental and calculated frequencies are listed in Table 2, which also includes a brief description of the type of motion.

The individual modes observed for both **1** and **2** and the contribution of each to the vibrational reorganization energy for the transition, $\lambda_v(q)$, were calculated using eqs 5 and 6 and appear in Figure 4 and Table 3.[46,47]
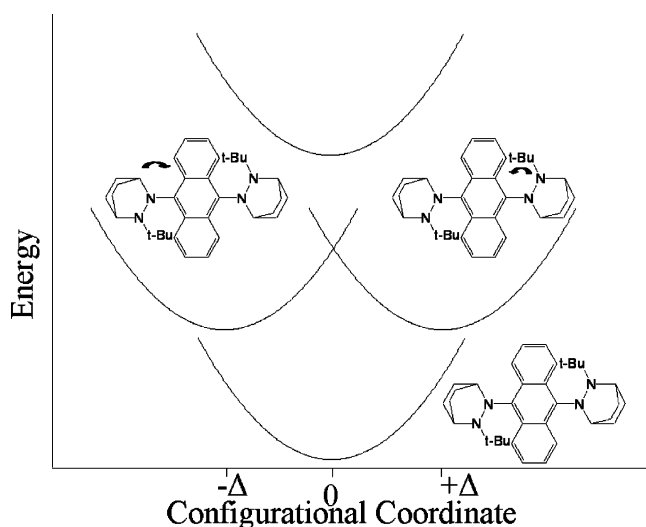
$$\frac{I_k}{I_{k'}} = \frac{\Delta_k^2 \omega_k^2}{\Delta_{k'}^2 \omega_{k'}^2} \tag{5}$$

$$\lambda_v(q) = (1/2)\Delta^2 \omega(q) \tag{6}$$

The total λ_v values are 5091 cm^{-1} for **1** and 2007 cm^{-1} for **2**. Thus, although the total amount of charge transferred to the anthracene ring is presumably greater for **2** than for **1**, because the transition is less endoenergetic (by about 2000 ± 100 cm^{-1} in solution and 2750 cm^{-1} in a KBr pellet, see Table 1), the reorganization energy for photoexcitation of **2** is only 39% as large as for **1**. The principal contributions to λ_v arise from distortions in the hydrazine groups. Because there are two hydrazines to spread the distortion over in **2**, smaller distortions occur in each and lower λ because λ increases as the square of the distortion.

TABLE 3: Comparison of Resonance Raman Modes and Reorganization Energies for Mono- and Dihydrazine-Substituted Anthracenes (1 and 2)

1 (HyAN)[a]		2 (Hy$_2$AN)	
$\omega(q)$ (cm^{-1})	$\lambda_v^{sym}(q)$ (cm^{-1})	$\omega(q)$ (cm^{-1})	$\lambda_v^{sym}(q)$ (cm^{-1})
241	157	220	6
		246	32
325	198		
392	442	390	211
410	211	417	94
463	456	462	240
558	143		
605	138	606	128
620	121	626	78
659	912	673	237
689	218		
713	149	715	124
1019	54	1026	90
1030	23	1036	63
1159	143	1130	86
1212	129		
1227	72		
1243	108	1242	94
1276	76	1265	122
1351	69		
1403	796	1398	219
1552	236	1527	56
		1547	124
1620	239		

[a] Data used from ref 14.

Figure 5. Excited-state mixed valence model. The two middle surfaces that are displaced in opposite directions on the configurational coordinate relative to the ground state represent the states resulting from hydrazine to anthracene charge transfer.

2. Excited-State Mixed Valence (ESMV). ESMV can be considered using the diabatic surfaces shown in Figure 5. The lowest-energy potential surface represents the ground electronic state. Absorption of a photon transfers charge from one of the hydrazine units to an empty π antibonding orbital localized primarily on the anthracene ring. The two upper diabatic potential energy surfaces represent excited states where the change has been transferred from the hydrazine on the left or the hydrazine on the right. These two surfaces along the asymmetric coordinate represent the two valence trapped mixed-valence states having equal energies vertically above the ground state minimum but distorted in opposite directions.

A prior spectroscopic study of **1**, which contains only one **Hy** charge-bearing unit, showed that the lowest energy electronic transition is from the hydrazine-centered HOMO (a π*(NN)-dominated MO) to the anthracene ring LUMO.[15] Electrooptical absorption measurements showed that the change in dipole moment vector is directed nearly parallel to the transition dipole moment vector, and that the electron-transfer distance on the diabatic surfaces is a rather modest 1.27 ± 0.06 Å, smaller than the 1.43 ± 0.08 Å obtained for the slightly less twisted 1-substituted naphthalene **3** and the 2.06 ± 0.04 Å for the 2-substituted naphthalene **4**. The ring carbon p orbital and nitrogen lone pair twist angles ϕ_{CN} were found to be 50° and 37°, respectively, by X-ray crystallography, in the same order as the electron-transfer distances. Increasing the twist lowers the electronic coupling, which is expected to be proportional to $\cos\phi_{CN}$, decreasing the amount of electron-transfer character of the transitions. The HOMO and LUMO of **2** are similar in character to those of **1**, and the ϵ_{max} for the first absorption band of **2** is 1.60 times that of **1**, slightly less than the statistical factor of 2 for the number of hydrazine units.

From the molecular orbital analysis, **2** might be expected to be a good case for using the ESMV model indicated in Figure 5. In the model, the ground state is a harmonic surface with its minimum at zero along the asymmetric vibrational coordinate, and the upper diabatic states are two harmonic surfaces with minima at $+\Delta$ and $-\Delta$ on the asymmetric vibrational coordinates. An electronic coupling between the diabatic excited states, H_{eff}, will produce two adiabatic surfaces with a splitting of $2H_{eff}$ at zero on the asymmetric configurational coordinate. The structure of the molecule determines that the transition dipole moment of ground state to upper diabatic transition dipole moments are nearly opposite in the direction. From previously studied cases,[15,24−30] one transition should be strongly forbidden, and only one main peak is expected in the absorption spectra and Raman excitation profile. This proved to be the case for the absorption spectrum but not for the Raman excitation profile (see Figure 3). The Raman excitation profile has a distinct dip between the main peak and branch peak at about 20 700 cm^{-1} for each mode. This unexpected dip found in the resonance Raman excitation profile suggested that the two-state ESMV model does not suffice for this molecule.

As we have pointed out in discussing the neighboring orbital model,[25,28,31] a minimum of four states are actually involved in a model that could produce reasonable electronic couplings, because the equal energy diabatic surfaces must enter into interactions with the bridge MOs in symmetric and antisymmetric combinations, which can only interact with symmetric and antisymmetric bridge MOs respectively. This leads to a pair of nested two-state models that share a common energy for the diabatic charge-bearing unit combination orbitals, as illustrated in the neighboring orbital diagram for **2** shown in Figure 6. It shows B3LYP/6-31G* MO pictures for the adiabatic orbitals of **2** in the center, and diabatic orbitals represented by MO pictures of pairs of hydrazines with the aryl group replaced by H on the left, and of anthracene, the bridge with the hydrazines replaced by H on the right. It will be noted that the highest energy adiabatic neighboring orbital (E$_4$, which is the **2** LUMO) is heavily anthracene-centered because of the large energy gap between the diabatic hydrazine combination orbitals and the upper diabatic bridge orbital, so that its two-state partner E$_2$ (which is the **2** (HOMO-1)) is very heavily hydrazine-centered. The antisymmetric hydrazine combination orbital mixes with the anthracene HOMO, producing the second pair, E$_3$ (the **2** HOMO) and E$_1$ (the **2** (HOMO-2)).

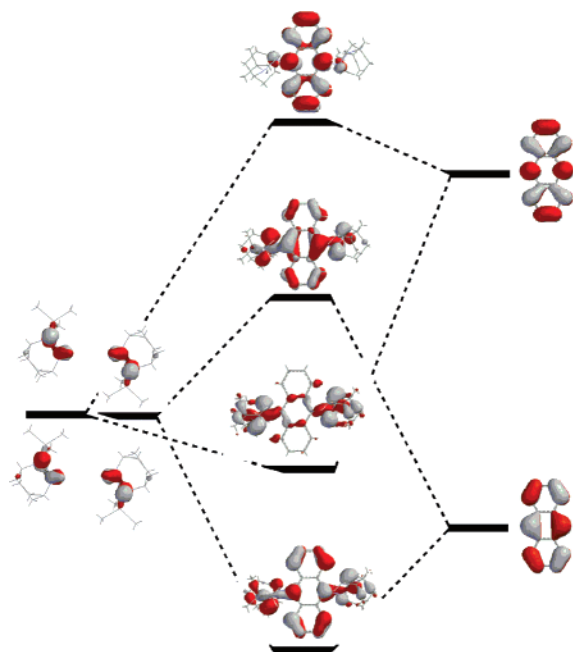**3. Origin of the Resonance De-Enhancement Dip.** Resonance Raman de-enhancement has been recognized and analyzed

Resonance Raman De-Enhancement

J. Phys. Chem. A, Vol. 111, No. 25, 2007 **5445**

Figure 6. Neighboring orbital analysis of **2**.

Figure 7. Calculated resonance Raman excitation profile (upper panel) and absorption spectrum (lower panel) superimposed on the experimental data.

quantitatively for several organometallic molecules in which a weakly allowed absorption band overlaps an allowed band.[48−52] In the excitation profile, a loss of intensity is observed in the region of the forbidden band. Its origin lies in the fact that resonance Raman profile for two or more states is given by the square of the sum of the polarizabilities as shown in eq 7 for two states

$$I_{i \to f} \propto \omega_I \omega_s^3 \left| \sum_{r=1}^{2} \alpha_r \right|^2 \tag{7}$$

where $\hbar\omega_I$ is the incident radiation energy, $\hbar\omega_s$ is the scattered radiation energy, and α_r is the resonance Raman scattering polarizability of rth adiabatic surfaces. When the real and imaginary parts of α_r from one state have opposite signs from that of another, cancellation can occur leading to loss of intensity in the wavelength region where the bands overlap. The absorption spectrum is the sum of the cross sections from the individual states and thus contains a weak increase in the region of the weakly allowed transition.

The de-enhancement in the experimentally determined profile shown in Figure 3 and the absorption spectrum (which does not contain unusual features at the wavelength of the dip in the rR profile) could not be modeled using only the intense dipole allowed and weak vibronically allowed ESMV bands. Displacements and transition dipole moments that gave rise to the prominent dip in the Raman excitation profile were accompanied by a new peak in the absorption spectrum. The model that was used successfully to calculate the profiles and absorption spectra includes all three of the excited states arising from transitions between the orbitals shown in Figure 6.

The simplest application of the model involves one vibrational coordinate, chosen to be the most highly displaced mode, the 390 cm^{-1} in-plane anthracene deformation. The potential energy matrix in the diabatic basis is

$$\begin{pmatrix} \frac{1}{2}k_Q(Q - \Delta Q_1)^2 + 16500 & 1500 & 200 \\ 1500 & \frac{1}{2}k_Q(Q - \Delta Q_2)^2 + 16500 & 200 \\ 200 & 200 & \frac{1}{2}k_Q(Q - \Delta Q_3)^2 + 21050 \end{pmatrix}$$
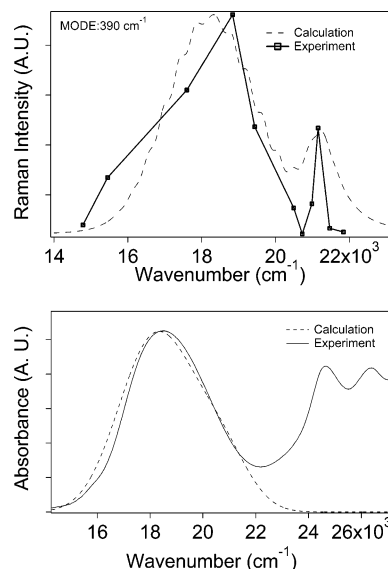
where $(k_Q = 4\pi^2 cM/(6.02 \times 10^{23}h))\omega^2$ (ω in units of cm^{-1}) is the force constant along coordinate Q, c is the speed of light, $M = 16$ is the reduced mass, h is Planck's constant, E_j is the energy of the potential minimum for jth state, $\omega = 390$ cm^{-1}, $\Delta Q_1 = \Delta Q_2 = 0.3$ Å, and $\Delta Q_3 = 0.001$ Å. The coupling between the diabatic states shown in Figure 5 is 1500 cm^{-1} and the coupling to the upper state is 200 cm^{-1}. After diagonalizing this matrix, the two lowest-energy surfaces that produce the overlapping absorption bands were used to calculate the de-enhancement. In the model that best fits the excitation profile, the transition dipole moment from the ground state to the upper adiabatic surface was 40% as large as that from the ground state to the lowest adiabatic surface. The calculated excitation Raman profile and the calculated absorption spectrum are shown in Figure 7.

The calculated spectra reproduce the sharp dip in the resonance Raman excitation profile and the single broad peak in the absorption spectrum. The parameters used to fit the spectrum are probably not unique, but they show that experimental vibrational data and reasonable values of the displacements can explain the origin of the dip in the rR profiles and its absence in absorption spectrum.

To explain the origin of the dip, the real and imaginary components of the resonance Raman scattering polarizability α for those two excited electronic states are shown in Figure 8. The cancellation of the imaginary part at 21 000 cm^{-1} and the cancellation of the real part at 20 000 cm^{-1} causes the de-enhancement of the two excited states. Another uncommon result was that the shape of real and imaginary parts of resonance Raman scattering polarizability α of upper electronic state are narrower in the three-state than in the two-state model. Since absorption intensity is proportional to absorption cross section while Raman intensity is proportional to the square of Raman scattering polarizability, it is conceivable that a narrower shape would lead to a narrower and more intense branch peak on the resonance Raman excitation profile. Therefore, the resonance excitation profile will have the dip effect while the absorption spectra are not sensitive enough to show the dip.

To extend the model, profiles for two modes, the 390 cm^{-1} mode discussed above and a high-frequency mode, the 1398 cm^{-1} anthracene carbon−hydrazine nitrogen stretch, were
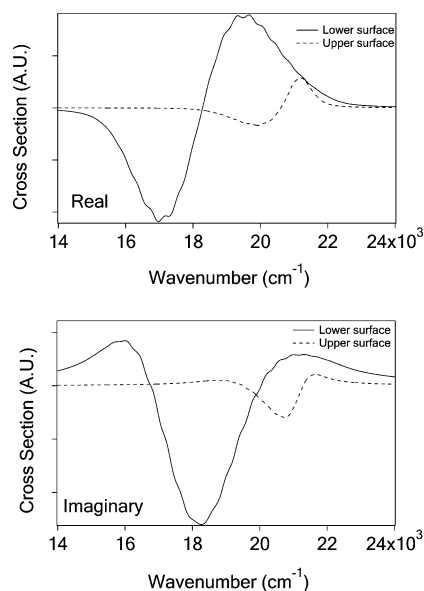
Figure 8. Real and imaginary components of the resonance Raman scattering polarizability α for two excited electronic states in three-state model.

calculated. In the two dimension calculation, coordinates Q and R represent the low and high-frequency modes, respectively.

The potential energy matrix is

$$\begin{vmatrix} \frac{1}{2}k_Q(Q-\Delta Q_1)^2 + & 1700 & 100 \\ \frac{1}{2}k_R(R-\Delta R_1)^2 + 17070 & & \\ 1700 & \frac{1}{2}k_Q(Q-\Delta Q_2)^2 + & 100 \\ & \frac{1}{2}k_R(R-\Delta R_2)^2 + 17070 & \\ 100 & 100 & \frac{1}{2}k_Q(Q-\Delta Q_3)^2 + \\ & & \frac{1}{2}k_R(R-\Delta R_3)^2 + 20750 \end{vmatrix}$$

where $\omega = 1398$ cm^{-1} is used in calculating k_R, $\Delta Q_1 = \Delta Q_2 = 0.27$ Å, $\Delta Q_3 = 0.001$ Å, $\Delta R_1 = \Delta R_2 = 0.03$ Å, and $\Delta R_3 = 0.05$ Å. The excitation profiles were calculated using the two overlapping states as discussed above. The calculated profiles, which are shown in Figure 9, are in reasonable agreement with the experiment and reproduce reasonably well the positions of the peaks and the dip.

Summary

The lowest excited states of **1** and **2** arise from hydrazine-to-anthracene charge transfer. Molecular orbital calculations show that the homo has a predominantly hydrazine π character and that the lumo is almost entirely anthracene π^* in character. The excited-state of the di-substituted compound **2** is mixed valence with antiparallel transition dipole moments resulting in dipole-allowed and vibronic allowed components separated in energy by twice the coupling. The two components overlap resulting in a broad, featureless absorption band. However, resonance Raman excitation profiles taken in resonance with the charge transfer absorption band revealed the presence of the weak component by a strong resonance de-enhancement.

The excitation profiles were used to obtain detailed information about the bond length and angle changes that occur as a result of the charge transfer. The largest distortions occur on the anthracene unit resulting from populating the three-node π^* orbital. In addition, large distortions on the hydrazines are found;
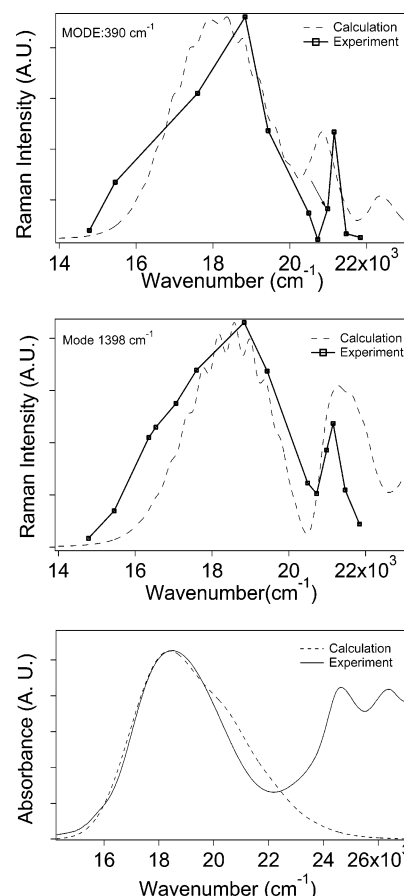

Figure 9. Two-dimension calculation of the resonance Raman excitation profile (upper panel) and the absorption spectrum of **2** using the 390 and 1398 cm^{-1} modes.

oxidizing them removes an NN π^* electron that shortens the NN bond length, flattens the nitrogens, and changes the electronic preference for twist at the NN bond from nearly 90° to 0°. The magnitudes of the normal coordinate changes are calculated using the time-dependent theory of resonance Raman spectroscopy.

The resonance de-enhancement observed in the rR excitation profile results from the fact that the resonance Raman profile for two or more states is given by the square of the sum of the polarizabilities for two states. When the real and imaginary parts of α_r from one state have opposite signs from that of another, cancellation can occur leading to loss of intensity in the wavelength region where the bands overlap. The absorption spectrum is the sum of the cross sections from the individual states and thus contains a weak increase in the region of the weakly allowed transition that is hidden by the breadth of the absorption bands. The de-enhancement was calculated using a model based on the states arising from the neighboring orbital model. Its presence provides more detail about the mixed valence excited state (including the magnitude and sign of the effective coupling) than is present in the broad, featureless ESMV absorption band.

References and Notes

(1) Endicott, J. F. In *Electron Transfer in Chemistry*; Wiley-VCH: Weinheim, Germany, 2001; Vol. 1, pp 238−270.

(2) Hubig, S. M.; Kochi, J. K. In *Electron Transfer in Chemistry*; Balzani, V., Astruk, D., Eds.; Wiley-VCH: Weinheim, Germany, 2001; Vol. 2, pp 518−676.

(3) Paddon-Row, M. N. In *Electron Transfer in Chemistry*; Balzani, V., Ed.; Wiley-VCH: Weinheim, Germany, 2001; Vol. 3, pp 179−271.

(4) Henbest, K.; Rodgers, M. A. J. In *Electron Tranfer in Chemistry*; Balzani, V., Astruk, D., Eds.; Wiley-VCH: Weinheim, Germany, 2001; Vol. 1, pp 558−588.

(5) Reber, C.; Zink, J. I. *Comments Inorg. Chem.* **1992**, *13*, 177.

(6) Shin, K.-S. K.; Zink, J. I. *Inorg. Chem.* **1989**, *28*, 4358.

(7) Wexler, D.; Zink, J. I.; Reber, C. In *Electronic and Vibronic Spectra of Transition Metal Complexes I*; Yersin, H., Ed.; Springer-Verlag: Berlin, 1994; Vol. 174.

(8) Acosta, A.; Zink, J. I. *J. Organomet. Chem.* **1998**, *554*, 87.

(9) Myers, Kelley, A. *J. Phys. Chem. A* **1999**, *103*, 6891.

(10) Myers, A. B. In *Laser Techniques in Chemistry*; Myers, A., Rizzo, T. R., Eds.; Wiley: New York, 1995; Vol. 23, p 325.

(11) Myers, A. B. *Chem. Rev.* **1996**, *96*, 911.

(12) Myers, A. B. *Acc. Chem. Res.* **1997**, *30*, 519.

(13) Nelsen, S. F.; Ismagilov, R. F.; Powell, D. R. *J. Am. Chem. Soc.* **1998**, *120*, 1924.

(14) Valverde-Aguilar, G.; Wang, X.; Nelsen, S. F.; Zink, J. I. *J. Am. Chem. Soc.* **2006**, *128*, 6180.

(15) Nelsen, S. F.; Konradsson, A. E.; Weaver, M. N.; Guzei, I.; Gobel, M.; Wortmann, R.; Lockard, J. V.; Zink, J. I. *J. Phys. Chem. A* **2005**, *109*, 10854.

(16) Hush, N. S. *Prog. Inorg. Chem.* **1967**, *8*, 391.

(17) Hush, N. S. *Coord. Chem. Rev.* **1985**, *64*, 135.

(18) Nelsen, S. F.; Ismagilov, R. F.; Powell, D. R. *J. Am. Chem. Soc.* **1996**, *118*, 6313.

(19) Nelsen, S. F.; Ismagilov, R. F.; Powell, D. R. *J. Am. Chem. Soc.* **1997**, *119*, 10213.

(20) Nelsen, S. F.; Ismagilov, R. F.; Gentile, K. E.; Powell, D. R. *J. Am. Chem. Soc.* **1999**, *121*, 7108.

(21) Nelsen, S. F.; Konradsson, A. E.; Teki, Y. *J. Am. Chem. Soc.* **2006**, *128*, 2902.

(22) Nelsen, S. F.; Ismagilov, R. F. *J. Phys. Chem. A* **1999**, *103*, 5373.

(23) Nelsen, S. F. *Adv. Phys. Org. Chem.* **2006**, *41*, 183.

(24) Lockard, J. V.; Zink, J. I.; Konradsson, A. E.; Weaver, M. N.; Nelsen, S. F. *J. Am. Chem. Soc.* **2003**, *125*, 13471.

(25) Nelsen, S. F.; Weaver, M. N.; Telo, J. P.; Zink, J. I. *J. Am. Chem. Soc.* **2005**, *127*, 10611.

(26) Nelsen, S. F.; Luo, Y.; Weaver, M. N.; Lockard, J. V.; Zink, J. I. *J. Org. Chem.* **2006**, *71*, 4286.

(27) Lockard, J. V.; Zink, J. I.; Trieber, D. A. I.; Konradsson, A. E.; Weaver, M. N.; Nelsen, S. F. *J. Phys. Chem. A* **2005**, *109*, 1205.

(28) Lockard, J. V.; Valverde, G.; Neuhauser, D.; Zink, J. I.; Luo, Y.; Weaver, M. N.; Nelsen, S. F. *J. Phys. Chem. A* **2006**, *110*, 57.

(29) Lockard, J. V.; Zink, J. I.; Luo, Y.; Weaver, M. N.; Konradsson, A. E.; Fowble, J. W.; Nelsen, S. F. *J. Am. Chem. Soc.* **2006**, *128*, 16524.

(30) Plummer, E. A.; Zink, J. I. *Inorg. Chem.* **2006**, *45*, 6556.

(31) Nelsen, S. F.; Weaver, M. N.; Luo, Y.; Lockard, J. V.; Zink, J. I. *J. Chem. Phys.* **2006**, *324*, 195.

(32) Zink, J. I.; Shin, K.-S. K. In *Advances in Photochemistry*; Volman, D. H.; Hammond, G. S.; Neckers, D. C., Eds.; Wiley: New York, 1991; Vol. 16, p 119.

(33) Lee, S.-Y.; Heller, E. J. *J. Chem. Phys.* **1979**, *71*, 4777.

(34) Heller, E. J.; Sundberg, R. L.; Tannor, D. J. *J. Phys. Chem.* **1982**, *86*, 1822.

(35) Tannor, D. J.; Heller, E. J. *J. Phys. Chem.* **1982**, *77*, 202.

(36) Heller, E. J. *Acc. Chem. Res.* **1981**, *14*, 368.

(37) Hanna, S. D.; Zink, J. I. *Inorg. Chem.* **1996**, *35*, 297.

(38) Wootton, J. L.; Zink, J. I. *J. Phys. Chem.* **1995**, *99*, 7251.

(39) Reber, C.; Zink, J. I. *J. Chem. Phys.* **1992**, *96*, 2681.

(40) Henary, M.; Zink, J. I. *J. Am. Chem. Soc.* **1989**, *111*, 7407.

(41) Henary, M.; Wootton, J. L.; Khan, S. I.; Zink, J. I. *Inorg. Chem.* **1997**, *36*, 796.

(42) Feit, M. D.; Fleck, J. A.; Steiger, A. *J. Comput. Phys.* **1982**, *47*, 412.

(43) Kosloff, D.; Kosloff, R. J. *J. Comput. Phys.* **1983**, *52*, 35.

(44) Tanner, J. J. *J. Chem. Educ.* **1990**, *67*, 917.

(45) Frisch, M. J.; Trucks, G. W.; Schlegel, H. B.; Scuseria, G. E.; Robb, M. A.; Cheeseman, J. R.; Montgomery, J. A., Jr.; Vreven, T.; Kudin, K. N.; Burant, J. C.; Millam, J. M.; Iyengar, S. S.; Tomasi, J.; Barone, V.; Mennucci, B.; Cossi, M.; Scalmani, G.; Rega, N.; Petersson, G. A.; Nakatsuji, H.; Hada, M.; Ehara, M.; Toyota, K.; Fukuda, R.; Hasegawa, J.; Ishida, M.; Nakajima, T.; Honda, Y.; Kitao, O.; Nakai, H.; Klene, M.; Li, X.; Knox, J. E.; Hratchian, H. P.; Cross, J. B.; Bakken, V.; Adamo, C.; Jaramillo, J.; Gomperts, R.; Stratmann, R. E.; Yazyev, O.; Austin, A. J.; Cammi, R.; Pomelli, C.; Ochterski, J. W.; Ayala, P. Y.; Morokuma, K.; Voth, G. A.; Salvador, P.; Dannenberg, J. J.; Zakrzewski, V. G.; Dapprich, S.; Daniels, A. D.; Strain, M. C.; Farkas, O.; Malick, D. K.; Rabuck, A. D.; Raghavachari, K.; Foresman, J. B.; Ortiz, J. V.; Cui, Q.; Baboul, A. G.; Clifford, S.; Cioslowski, J.; Sefanov, B. B.; Liu, G.; Liashenko, A.; Piskorz, P.; Komaromi, I.; Martin, R. L.; Fox, D. J.; Keith, T.; Al-Laham, M. A.; Peng, C. Y.; Nanayakkara, A.; Challacombe, M.; Gill, P. M. W.; Johnson, B.; Chen, W.; Wong, M. W.; Gonzalez, C.; Pople, J. A. *Gaussian 03*, revision C.02; Gaussian, Inc.: Wallingford, CT, 2004.

(46) Tang, J.; Albrecht, A. C. In *Raman Spectroscopy*; Szynanshki, H., Ed.; Plenum: New York, 1970; Vol. 2, p 33.

(47) Warshel, A.; Dauber, P. *J. Chem. Phys.* **1977**, *66*, 5477.

(48) Reber, C.; Zink, J. I. *J. Phys. Chem.* **1992**, *96*, 571.

(49) Stein, P.; Miskowski, V.; Woodruff, W. H.; Griffin, J. P.; Werner, K. G.; Gaber, B. P.; Spiro, T. G. *J. Chem. Phys.* **1976**, *64*, 2159.

(50) Shin, K.-S. K.; Zink, J. I. *J. Am. Chem. Soc.* **1990**, *112*, 7148.

(51) Heather, R.; Jiang, X.-P.; Metiu, H. *Chem. Phys. Lett.* **1987**, *142*, 303.

(52) Heather, R.; Metiu, H. *J. Chem. Phys.* **1989**, *90*, 6903.